## Research Paper

# Stress relaxation behavior of tessellated cartilage from the jaws of blue sharks

CrossMark

**Xiaoxi Liu[a],\***, **Mason N. Dean[b]**, **Hamed Youssefpour[a]**, **Adam P. Summers[c]**, **James C. Earthman[a]**

[a]Department of Chemical Engineering and Materials Science, 916 Engineering Tower, University of California, Irvine, CA 92697-2575, USA
[b]Department of Biomaterials, Max Planck Institute of Colloids and Interfaces, 14424 Potsdam, Germany
[c]Friday Harbor Labs, University of Washington, Friday Harbor, WA 98250, USA

ABSTRACT

Much of the skeleton of sharks, skate and rays (Elasmobranchii) is characterized by a tessellated structure, composed of a shell of small, mineralized plates (tesserae) joined by intertesseral ligaments overlaying a soft cartilage core. Although tessellated cartilage is a defining feature of this group of fishes, the significance of this skeletal tissue type – particularly from a mechanical perspective – is unknown. The aim of the present work was to perform stress relaxation experiments with tessellated cartilage samples from the jaws of blue sharks to better understand the time dependent behavior of this skeletal type.

In order to facilitate this aim, the resulting relaxation behavior for different loading directions were simulated using the transversely isotropic biphasic model and this model combined with generalized Maxwell elements to represent the tessellated layer. Analysis of the ability of the models to simulate the observed experimental behavior indicates that the transversely isotropic biphasic model can provide good predictions of the relaxation behavior of the hyaline cartilage. However, the incorporation of Maxwell elements into this model can achieve a more accurate simulation of the dynamic behavior of calcified cartilage when the loading is parallel to the tessellated layer. Correlation of experimental data with present combined composite models showed that the equilibrium modulus of the tessellated layer for this loading direction is about 45 times greater than that for uncalcified cartilage. Moreover, tessellation has relatively little effect on the viscoelasticity of shark cartilage under loading that is normal to the tessellated layer.

© 2013 Elsevier Ltd. All rights reserved.

## 1. Introduction

Cartilage is both stiff and resilient, an ideal contour filler and bearing surface that minimizes contact stresses generated during compressive loading and contributes to lubrication mechanisms in the joint (Hall, 2005; Hunziker, 1999). In most vertebrates, whereas bones provide a rigid framework for the body, cartilage exists in much smaller quantity, providing flexible and elastic structural support, primarily in the joints. One exception is found in the elasmobranch fishes (sharks,

rays and their relatives), whose skeletons are made entirely of cartilage, which therefore must perform both the functions carried out by mammalian bone as well as typical functions of mammalian cartilage (Dean et al. 2009; Macesic and Summers, 2012). However, possession of a fully cartilaginous skeleton clearly does not compromise behaviors, as elasmo-branchs are among the fastest and largest animals in the oceans, and many species can feed on prey larger than themselves or protected by turtle or mollusk shell, which can be harder than cortical bone. Furthermore, the skeleton is cyclically loaded, perhaps $10^6$–$10^{10}$ times over an animal's lifetime without failure (Ashhurst, 2004). A key aspect that apparently makes this high level of performance possible is the "tessellation" of the shark skeleton, a composite of mineralized blocks of hydroxyapatite (tesserae) joined by intertesseral ligaments over a core of uncalcified cartilage (Clement, 1992; Dingerkus et al., 1991; Kemp and Westrin, 1979; Moss, 1977; Dean and Summers, 2006). An example of this tissue is illustrated in Fig. 1 with a corresponding photograph (inset).

The specific role of tessellation in the high performance and safety factors of elasmobranch skeletons is unknown and to date has only been addressed theoretically. Wroe et al. (2008) multi-material finite-element (FE) models of bite force in the white shark (*Carcharodon carcharias*) took into account the composite nature of the skeleton, When compared with a hypothetical shark with bony jaws, the modeled cartilaginous jaws exhibited lower stress, but greater deformation and strain; however the use of cartilage rather than bone showed no apparent impediment to the generation of high bite forces. Liu et al. (2010) developed an analytical composite model to simulate the bending behavior of tessellated cartilage, incorporating anatomical dimensions for tesserae and intertesseral

joints, as well as the preliminary material property data for tissue components used in Wroe et al. (2008)'s FE-models. Liu et al.'s two-dimensional cross-sectional models demonstrate that the high fatigue resistance of elasmobranch skeletons could be accomplished in part by the tessellated layer's differential response to tensile vs. compressive loading. The modeled movement of the joints within the tesserae mat would allow the skeleton to manage stresses to avoid damage, ensuring that the majority of loading stresses are consolidated in the tesserae on the side of the skeleton loaded under compression, a mode more resistant to fatigue damage (Malzahn and Schultz, 1986; Hacker and Ansell, 2001). It is clear that the heterogeneity of this tissue (the combination of mineralized and unmineralized cartilage and fibrous material) and its tessellation play primary roles in the skeleton's mechanical properties, so both must be accounted for to truly characterize this composite tissue's response to loading and understand the contribution of individual components.

As elasmobranch uncalcified cartilage is surely highly viscoelastic (like mammalian cartilage), an effective method for understanding the effects of tessellation on cartilage is to describe the contributions of tissue compositeness and ani-sotropy (loading direction) to the viscoelastic response. Like mammalian articular cartilage, water is the most abundant component of the uncalcified portion of elasmobranch carti-lage, constituting up to 90% of its wet weight, while collagen and proteoglycans are the most abundant structural macro-molecule in ECM, comprising up to 50% and 70% of the dry weight of the uncalcified cartilage, respectively, for several shark species (Porter et al., 2013). Given these broad composi-tional similarities between uncalcified cartilage in mammals and elasmobranchs, previous viscoelastic analyses of mam-malian articular cartilage can provide vital reference for the
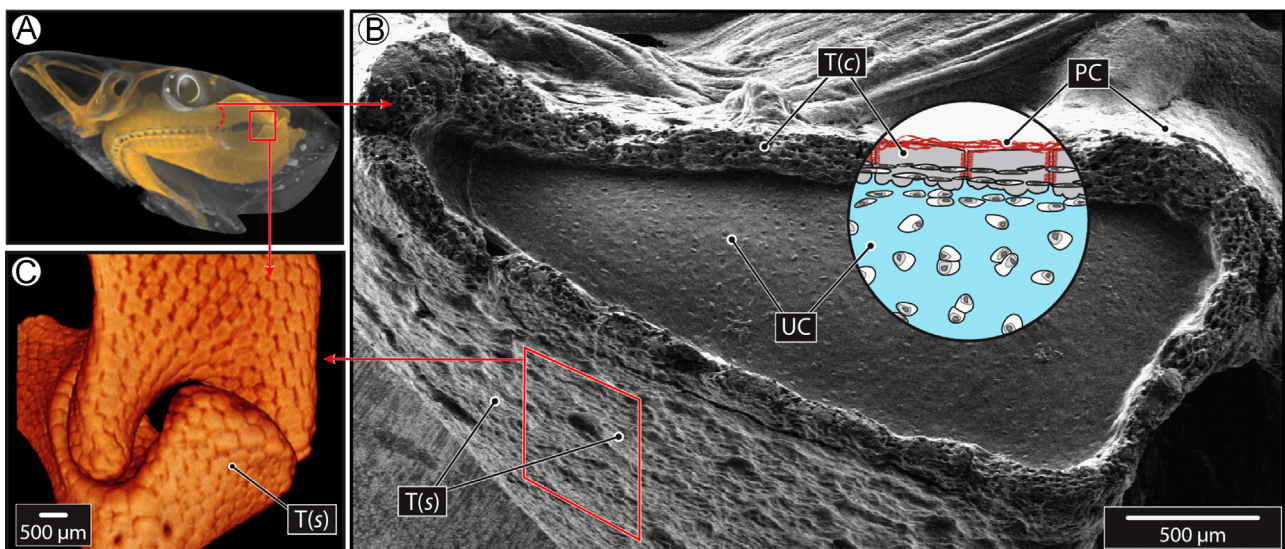


Fig. 1 – The tessellated cartilage of elasmobranch fishes. (A) CT scan of the blue shark, *P. glauca*, used in this study. A cross-section of the skeleton (B) shows uncalcified cartilage [UC] overlain by mineralized tesserae [T(c)] and fibrous perichondrium [PC]; the inset image provides a schematic view of the tissue relationships, as well as the fibrous joints between tesserae. The bottom left of the image shows a perspective on tesserae in surface aspect [T(s)], covered with perichondrium. The tiled tesseral covering is more obvious in a CT scan of a jaw joint (C), where the perichondrium is not visualized, and illustrates how tesserae cover the entire surface of the jaws, even on complex surfaces. (Cryo-SEM image in B from jaws of *Urobatis halleri*; jaw joint CT scan in C from *Urobatis jamaicensis*.).

effective modeling of the unmineralized phase of the tessellated skeleton. In Mow et al. (1980)'s biphasic theory, articular cartilage is treated as a binary mixture of an intrinsically incompressible solid phase, representing primarily the collagen fibers, proteoglycans, and chondrocytes, and an intrinsically incompressible fluid phase representing interstitial water. The time dependent deformation behavior of cartilage is thought to result primarily from the dissipative drag of interstitial fluid flowing through a porous solid matrix consisting of different fibers. Mow et al. (1980,1989), Mak and Mow (1987) first used a linear biphasic model to describe both creep and relaxation behaviors of articular cartilage in confined and unconfined compressive tests and indentation test. Their studies assert that the frictional forces acting on the solid phase, which correspond to the flow of the liquid phase, are governed by the tissue permeability, tissue thickness and interstitial hydro-static fluid pressure drop. However, the true anisotropic and inhomogeneous nature of the tissue and nonlinearities in finite deformation were not accounted for. To address these complexities, Cohen et al. (1993, 1998) demonstrated that a linear transversely isotropic biphasic theory could provide successful simulations of stress relaxation tests, suggesting that difficulties encountered with the isotropic model could be overcome by modeling tissue anisotropy. Alternatively, Mak (1986) proposed a biphasic poroviscoelastic model that accounts for the intrinsic viscoelasticity of the solid phase of the tissue. Suh and Bai (1998) were able to successfully use this approach in a finite element model to predict the relaxation behaviors of articular cartilage.

It stands to reason that the addition of a tessellated layer consisting of both tesserae and intertesseral joints may require a more involved constitutive model than that used to describe the behavior of articular cartilage. One possible solution is to approximate multiple component behavior of tessellated layer with a generalized Maxwell model, which has been used to simulate viscoelastic behavior of mineralized tissues, such as dentin (Kinney et al., 2003) and bones (Shepherd et al., 2011). The generalized Maxwell model contains a configuration of spring-dashpot elements that are arranged both in series and in parallel (Brinson and Brinson, 2007; Zhang et al., 2008) (Fig. 2). The ability for spring-dashpot Maxwell elements to be flexibly assembled in a variety of configurations allows models to be tuned to accurately reflect the actual relaxation behaviors of experimentally loaded tissues, while also permitting determination

of the relative contributions of viscous and non-viscous components of a tissue's mechanical response.

In the present work, our aim is to understand the viscoelastic behavior of shark uncalcified cartilage and tessellated cartilage via an interative experimental and modeling approach, allowing us to determine the relative contributions of each material to the behavior of the composite tissue. Our method is to introduce and compare a series of composite models that combine a biphasic model with variations on the generalized Maxwell formulation to simulate dynamic behavior of shark tessellated cartilage tested under unconfined stress relaxation and several sample orientations. Specifically, we hypothesized that the viscoelastic mechanical behavior of shark uncalcified cartilage may be quantitatively represented by the transversely linear biphasic model developed by Cohen et al. (1998) while the tessellated layer is simulated by the generalized Maxwell model. By comparing the relaxation responses of non-tessellated samples with those of tessellated samples loaded in two directions, we address the relative contributions of tissue components on viscous and non-viscous responses in the composite as a whole, while providing perspective into the functional consequences of surface tiling on a viscoelastic composite.

## 2.     Materials and tests

Both uncalcified cartilage and tessellated cartilage were obtained from the lower jaw of adult blue sharks (*Prionace glauca*) and cut into small uniform pieces using surgical blades. The thickness of all samples was reduced to about 6 mm using a rotary polishing machine. Then the samples were cut again to about 10 mm length and were polished with fine polishing paper (600 grit) to a uniform geometry of $10 \times 6 \times 6$ mm. All samples were stored at $-20\,^\circ$C and immersed in Ringers solution for 2hrs prior to testing. Ringers' solution, produced by dissolving 6.5 g NaCl, 0.42 g KCl, 0.25 g $CaCl_2$ and 1 mol of sodium bicarbonate in 1 l of distilled water, is used to maintain the swelling pressure of cartilage (Lu et al., 2007).

Stress relaxation tests were employed to examine the viscoelastic behavior of shark tessellated cartilage loaded in different orientations, with and without tessellation. The tests were performed with the samples in a small bath of Ringer's solution to avoid loss of interstitial fluid during the experiments. Relaxation behavior was measured by deforming each sample to a displacement of 5 mm using a computer that controls a motorized micrometer with a non-rotating tip and monitors the resulting force with an Interface SM-10 load cell (Interface Inc, Scottsdale, AZ). The load cell was interfaced to the computer equipped with a National Instruments Model PCI-6132 data acquisition card. The load data were acquired and recorded by custom software developed using the Labview visual programming environment (National Instruments Inc., Austin, TX, USA). The desired loading rate and displacement were imposed with an Anaheim Automation 17Y Stepper Motor, which is custom incorporated with the nonrotating micrometer using flexible couplings. The diameter of the micrometer tip is 6 mm. The data were acquired at 10 samples/s for the first 15 s and then at about 0.2 samples/s for the remaining time of each test. A higher
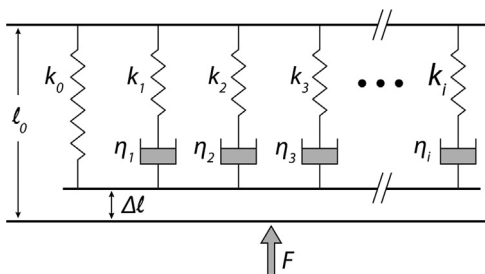


**Fig. 2 – Schematics of the generalized Maxwell model of viscoelastic behavior under a fixed compressive displacement, $\Delta l$ (Roylance, 2001).**

sampling rate at the beginning of each test was chosen to precisely determine the peak force and fast relaxation behavior after reaching the imposed displacement. For same type of samples, at least 8 relaxation tests were conducted to confirm the reproducibility of the experiment. All experimental data were processed using a piecewise 5-point smoothing method to reduce scatter in the data. A photograph of the relaxation test system used in the present work is shown in Fig. 3. The samples were tested with the loading in a direction either normal or parallel to the tessellated layer as illustrated schematically in Fig. 4. Because the tessellated layer occupies one face of tessellated samples and our aim was to ensure load
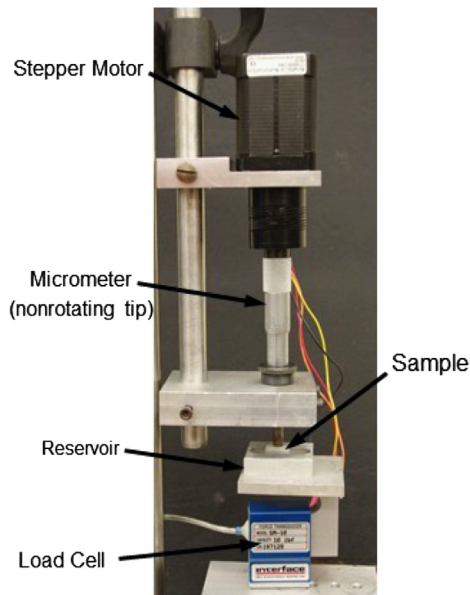
was applied within the plane of the tesseral mat, a surface-to-surface sample configuration shown was employed for parallel loading to provide symmetry of applied force and prevent the tessellated layers from buckling. For this configuration, two tessellated layers from the same piece of shark tissue were positioned adjacent to each other as shown in Fig. 4.

We note that the tessellated cartilage samples under parallel loading (TC-PL) were not loaded over the entirety of the hyaline cartilage for the dual samples (Fig. 4). To avoid errors in the calculation of viscoelastic properties using current test data, we introduced a series of preliminary tests to calibrate a correction factor (or constraint factor) to account for the selective loading on tessellated samples tested under parallel loading. Samples used in these tests were made from 6061 Alloy, silicone and Delrin® acetal resin each with known stiffness properties and the same dimensions as the shark cartilage samples, which were tested under the same loading conditions. Based on these tests, we found that each relaxation curve was approximately 1.15 times higher for two surface-to-surface samples compared to that for the corresponding material loaded over its entirety. Therefore, a correction factor of 1.15 was used for the analysis of stress relaxation behavior for tessellated cartilage under parallel loading.

As it is difficult to harvest thick pieces of cartilage with flat tessellated surfaces, our sample geometries somewhat dictated our testing regime; given the thickness of the samples, a low experimental displacement rate, 0.1 mm/s, was chosen to allow adequate time for data collection (faster rates resulted in the desired strain being reached too quickly to allow adequate data resolution and accurate analysis). To understand this displacement rate in the context of rates experienced by tessellated cartilage in vivo, we approximated biologically-relevant rates of tissue displacement during normal but rapid skeletal loading (e.g. during biting during a predation event),



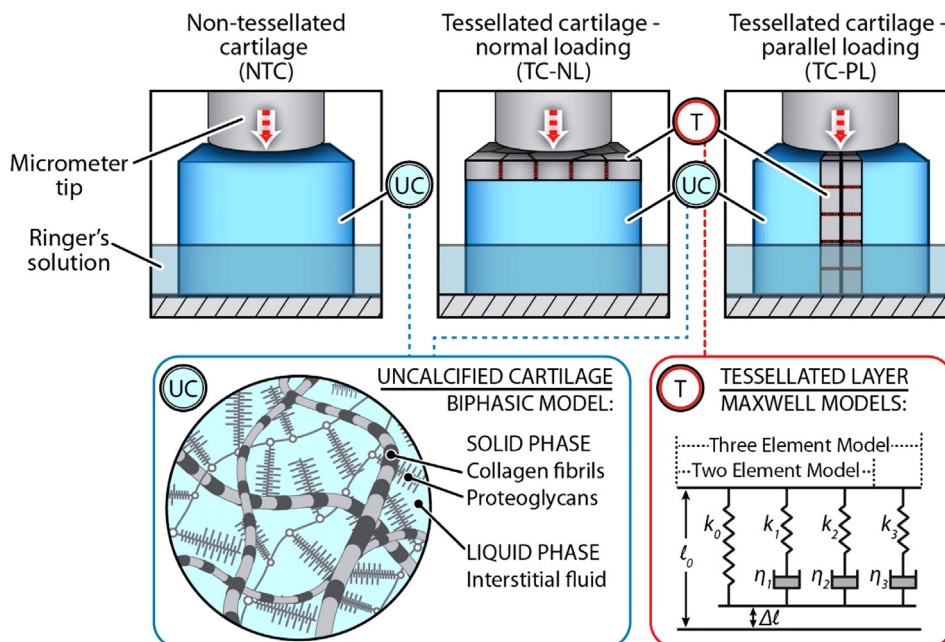Fig. 3 – Test configuration used for the present stress relaxation experiments.



Fig. 4 – Schematic of tessellated cartilage samples under normal and parallel loading, together with corresponding constitutive models used for data analysis.

using existing anatomical, material property and feeding performance data from two shark species with very different ecologies: the horn shark (*Heterodontus francisci*), a hard prey specialist, and the lemon shark (*Negaprion brevirostris*), a piscivore (Huber et al., 2005; Huber, 2006). We calculated the average rate of force development (300–470 N/s) during the closing phase of an anterior bite (the front of the jaw) from the rising slope of force vs. time curves for feeding events. The stress rate ($4.46$–$5.97 \times 10^6$ Pa/s) was then calculated by dividing the force rate by the cross-sectional area of the jaws at the bite point, measured from CT scans of animals using Amira software (VSG, Burlington, MA, USA). The stress rate was then divided by the stiffness of the jaw tissue for these species ($4.30$–$5.60 \times 10^7$ Pa, determined from stress relaxation tests of cylindrical plugs of uncalcified jaw tissue, Huber, unpublished data), to calculate strain rate (0.10–0.11 Pa/s), which was converted to displacement rate (0.87–1.65 mm/s) by multiplying by the height of the jaws at the bite point.

These calculated tissue displacement rates during feeding are several times higher than our experimental displacement rate, however it is important to note that the incorporated, species-specific values for tissue stiffness do not take into account the tessellated layer. Although the volume of the tessellated layer is small in comparison with the uncalcified core of the skeleton, Liu et al. (2010)'s anatomically-based analytical model indicates that the tesserae play a major role in determining overall skeletal stiffness. Given that preliminary nanoindentation tests show that the mineralized tissue of tesserae is as stiff as bone (10–30 GPa, determined from nanoindentation tests for *Urobatis halleri* jaw tesserae; Fix, et al., 2013), the Young's modulus of the tessellated skeletal tissue (the uncalcified and calcified cartilage composite) would be one to two orders of magnitude higher than the species-specific stiffness values for uncalcified cartilage listed above. With this higher stiffness, we would then expect our calculated species-specific displacement rates to be proportionately smaller (i.e. $\sim 1.25 \times 10^{-1}$–$1.25 \times 10^{-2}$ mm/s); our experimental rates are therefore likely biologically reasonable for tissue displacements during normal skeletal movements like biting.

## 3. Modeling

### 3.1. Transversely isotropic biphasic model for uncalicified cartilage

Cohen et al. (1998) developed a biphasic model for describing the viscoelastic behavior of hyaline cartilage, with the axis of transverse isotropy in the direction aligned with the collagen fiber. In transverse isotropy, the fourth order stiffness tensor, $C$, is characterized by five independent elastic constants: the elastic properties are Young's modulus and Poisson's ratio in the transverse plane ($E_1$ and $\nu_{21}$, respectively) and out-of-plane ($E_3$ and $\nu_{31}$, respectively) and the out-of-plane shear modulus ($G_{31}$), which is not used for the case of uniaxial compression, since no shear deformation occurs in the loading direction in the present models. The equations for total axial stress were derived from governing equations and

solved for the stress relaxation test using Laplace transforms and modified Bessel functions.

The loading history in the current stress relaxation experiments can be divided into two segments for which strain functions are defined. These functions are:

$$\varepsilon(t) = \dot{\varepsilon}(t - t_0) \quad \text{for the ramp segment} \tag{1}$$

$$\varepsilon(t) = \dot{\varepsilon}\, t_1 \quad \text{for the relaxation segment} \tag{2}$$

where $\dot{\varepsilon}$ is the constant strain rate during the ramp segment, $t$ is the duration of the ramp segment, and $t_0 = 0$ for the present test. The ramp displacement was terminated at time and the strain, given by Eq. (2), was held constant thereafter during the relaxation segment. The stress during the ramp portion of experiment described by a transversely isotropic biphasic model is

$$\sigma_C(t) = E_3 \dot{\varepsilon} t + E_1 \frac{\dot{\varepsilon} a^2}{C_{11} k} \Delta_3 \left\{ \frac{1}{8} - \sum_{n=1}^{\infty} \frac{\exp(A_n t)}{B_n} \right\} \tag{3}$$

and that during the relaxation portion (for $t > t_1$) is given by

$$\sigma_T(t) = E_3 \dot{\varepsilon} t_1 - E_1 \frac{\dot{\varepsilon} a^2}{C_{11} k} \Delta_3 \left\{ \sum_{n=1}^{\infty} \frac{\exp(A_n t) - \exp(A_n(t - t_1))}{B_n} \right\} \tag{4}$$

where $k$ is the permeability, which is indicative of the flow characteristics of the interstitial fluid, and $a$ is the diameter of the loading surface for the present experiments (Cohen et al., 1998). The constants in Eqs. (3) and (4) are defined as

$$C_{11} \equiv E_1 \Delta_2 / \Delta_1, \tag{5}$$

$$\Delta_1 \equiv 1 - \nu_{21} - 2\nu_{31}^2 E_1 / E_3, \tag{6}$$

$$\Delta_2 \equiv (1 - \nu_{31}^2 E_1 / E_3) / (1 + \nu_{21}), \tag{7}$$

$$\Delta_3 \equiv (1 - 2\nu_{31}^2) \Delta_2 / \Delta_1, \tag{8}$$

$$A_n \equiv -\alpha_n^2 C_{11} k / a^2, \tag{9}$$

$$B_n \equiv \alpha_n^2 [\Delta_2^2 \alpha_n^2 - \Delta_1 / (1 + \nu_{21})], \tag{10}$$

and $\alpha_n$ are roots of the equation:

$$J_1(x) - \left( \frac{1 - \nu_{31}^2 E_1 / E_3)}{1 - \nu_{21} - 2\nu_{31}^2 E_1 / E_3} \right) x J_0(x) = 0. \tag{11}$$

where $J_0$ and $J_1$ are Bessel functions of the first kind, and $x = \alpha_n$. Then the relaxation elasticity of hyaline cartilage can be calculated by differentiating Eq. (3) with respect to strain, which gives

$$E_C(t) = E_3 - E_1 \frac{a^2}{C_{11} k} \Delta_3 \sum_{n=1}^{\infty} \frac{A_n \exp(A_n t)}{B_n} . \tag{12}$$

The specimens tested in the present work were rectangular instead of cylindrical to avoid difficulties in the standardization of specimen preparation. Rectangular specimen geometries have been modeled successfully using this biphasic approach. For example, a biphasic and transversely isotropic model was applied to rectangular meniscus samples using a finite element approach (LeRoux and Setton, 2002). Their model provided good predictions of experimental data for stress relaxation tests, with coefficients of determination, $R^2 > 0.9$.

## 3.2. Generalized Maxwell model for tessellated layer

The relaxation function of a generalized Maxwell solid is typically determined using a Prony series (Chen, 2000):

$$Y(t) = Y_0 \left( 1 - \sum_{i=1}^{n} P_i (1 - e^{-(t/\tau_i)}) \right), \tag{13}$$

where $P_i$ is the ith Prony constant (i=1, 2, ....), $\tau_i$ is the ith relaxation time constant (i=1, 2, ...), $n$ is the number of Maxwell elements and $Y_0$ is the instantaneous response of the material, which is a constant for a given tissue, loading direction temperature and imposed strain. We assume that the relaxation elasticity of the tessellated layer can be represented by Prony's series as indicated by Eq. (13). It follows that the time dependent elastic modulus is given by

$$E_T(t) = E_0 \left( 1 - \sum_{i=1}^{n} P_i (1 - e^{-(t/\tau_i)}) \right). \tag{14}$$

where $E_0$ is the instantaneous modulus. For time $t=0$, $E_T(0) = E_0$ and for $t=\infty$, $E_T(\infty) = E_0 (1 - \Sigma Pi)$. $E(\infty)$ is the equilibrium modulus, which is the intrinsic time independent stiffness of the viscoelastic material (Lu et al., 2007; Armstrong et al., 1984).

## 3.3. Composite model for shark tessellated cartilage

To account for the additional complexity introduced by the calcified tessellated layer, we iteratively added additional Maxwell elements to the biphasic model described above (Fig. 4) to determine whether they improve the accuracy of simulating the relaxation behavior of this tissue. For viscoelastic materials, a superposition of hereditary integrals can be used to describe a time dependent response. If a specimen is deformation free prior to the time $t=0$ at which a strain $\varepsilon(t)$ is applied, the stress for time $t>0$ is given by Chen (2000)

$$\sigma = \int_0^t E(t-\delta) \frac{d\varepsilon(\delta)}{dt} d\delta. \tag{15}$$

where $d\varepsilon(\delta)/dt$ is the strain rate. We note that normal loading should predominantly result in isostress conditions while parallel loading should predominantly result in isostrain conditions between the tessellated and uncalcified cartilage layers as illustrated in Fig. 4. The equations governing the effective modulus for these two loading direction are

$$E_{eff}(t)_{isostress} = \left[ \frac{f_T}{E_T} + \frac{(1-f_T)}{E_C} \right]^{-1} = \frac{E_C}{1 + ((E_C/E_T)-1) \times f_T} \tag{16}$$

$$E_{eff}(t)_{isostrain} = f_T E_T + (1-f_T) E_C, \tag{17}$$

where $f_T$ is the volume fraction of tessellated layer, which is $E_T$ is the elastic modulus of the tessellated layer, and $E_C$ is the elastic modulus of the uncalcified cartilage. The volume fraction of the tessellated layer (fT) in the structure can be measured from the thickness ratio of tessellated layer to overall cartilage, which is approximately 0.1 for present samples. Substituting Eq. (12) (transversely isotropic biphasic model) for $E_C(t)$ and Eq. (14) (generalized Maxwell model) for $E_T(t)$ into Eqs. (16) and (17) and then substituting the resulting relation for the effective modulus under isostress condition into Eq. (15), the stress on tessellated cartilage under normal

loading is given by: $0 < t < t_1$ :

$$\sigma(t) = \int_0^t \frac{E_3 - E_1(a^2/C_{11}k)\Delta_3 \sum_{n=1}^{\infty} (A_n \exp(A_n(t-\delta))/B_n)}{1 + \left( \frac{E_3 - E_1(a^2/C_{11}k)\Delta_3 \sum_{n=1}^{\infty} (A_n \exp(A_n(t-\delta))/B_n)}{E_0(1 - \sum_{i=1}^{n} P_i(1 - e^{-((t-\delta)/\tau_i)}))} - 1 \right) \times f_T} \dot{\varepsilon} d\delta, \tag{18}$$

$t > t_1$:

$$\sigma(t) = \int_0^{t_1} \frac{E_3 - E_1(a^2/C_{11}k)\Delta_3 \sum_{n=1}^{\infty} (A_n \exp(A_n(t-\delta))/B_n)}{1 + \left( \frac{E_3 - E_1(a^2/C_{11}k)\Delta_3 \sum_{n=1}^{\infty} (A_n \exp(A_n(t-\delta))/B_n)}{E_0(1 - \sum_{i=1}^{n} P_i(1 - e^{-((t-\delta)/\tau_i)}))} - 1 \right) \times f_T} \dot{\varepsilon} t_1 d\delta \tag{19}$$

Similarly, the mean stress for tessellated cartilage under parallel loading is then: $0 < t < t_1$:

$$\sigma(t) = f_T \left( E_3 \dot{\varepsilon} t + E_1 \frac{\dot{\varepsilon} a^2}{C_{11} k} \Delta_3 \left\{ \frac{1}{8} - \sum_{n=1}^{\infty} \frac{\exp(A_n t)}{B_n} \right\} \right)$$
$$+ (1-f_T) E_0 \dot{\varepsilon} (t - \sum_{i=1}^{n} p_i t + \sum_{i=1}^{n} p_i \tau_i + \sum_{i=1}^{n} p_i \tau_i \exp(-(t/\tau_i))), \tag{20}$$

$t > t_1$:

$$\sigma(t) = f_T \left( E_3 \dot{\varepsilon} t_1 - \frac{E_1 \dot{\varepsilon} a^2}{C_{11} k} \Delta_3 \left\{ \sum_{i=1}^{\infty} \frac{\exp(A_n t) - \exp(A_n(t-t_1))}{B_n} \right\} \right)$$
$$+ (1-f_T) E_0 \dot{\varepsilon} (t_1 - \sum_{i=1}^{n} p_i t_1 + \sum_{i=1}^{n} p_i \tau_i \exp(-((t-t_1)/\tau_i))$$
$$- \sum_{i=1}^{n} p_i \tau_i \exp(-(t/\tau_i))). \tag{21}$$

The correlations between experimental data and model results were determined using non-linear least squares regression analysis ($p=0.05$). For uncalcified cartilage, we note that from Eqs. (3) and (4) that there are five material coefficients: $v_{21}$, $v_{31}$, $E_1$, $E_3$ and $k$. These material parameters were determined as follows. First, the equilibrium modulus, $E_3$, was calculated using the equilibrium stress and strain values (when $t>3000$ s for current relaxation tests). Next, a nonlinear least-squares regression method was used to fit the remaining material parameters $v_{21}$, $v_{31}$, $E_1$ and $k$ to for both ramp and relaxation. A master table for the roots of $xJ_0(x)$ and $J_1(x)$ was then created. Based on this table, the bisection method was used to calculate each $\alpha_n$ where eight terms were used (Yin and Elliott, 2004). For tessellated cartilage, we substituted the biphasic properties of the uncalcified cartilage samples for this component in the composite model except for the permeability, which we assume can be influenced by the introduction of the tessellated layer.

For faster ramps, both the ramp and the early portion of the relaxation should not be included in regression analysis due to transient effects (Lakers and Vanderby, 1999; Yin and Elliott, 2004). Based on the 2.5 s ramp time, we chose to model the relaxation starting at 5 s to ensure that transient effects did not have a dominant influence on our data. In order to achieve a full representation of both short term and long term relaxing mechanisms of viscoelastic materials, one-element, two-element and three-element generalized Maxwell terms were incorporated to describe the observed behavior.

## 4. Results

Both load ramp and relaxation curves are plotted in Fig. 5a and b for all three test configurations. The stress relaxation data for uncalcified cartilage and tessellated cartilage under normal loading were very similar while the stress for parallel

loading (in-plane direction) for tessellated cartilage indicated substantially higher stress resulting from a greater overall stiffness. The average regression results for the relaxation behavior of uncalcified non-tessellated cartilage (NTC) using the transversely isotropic biphasic model are listed in Table 1. The accuracy of this model (dashed) for a representative relaxation response (solid) is demonstrated in Fig. 6a. The model described the majority of variation in experimental data, with a coefficient of determination, $R^2$, greater than 0.987 (Table 1). Thus, it appears that the time dependent response of the shark hyaline cartilage can be simulated reasonably well by the transversely isotropic biphasic model. The average instantaneous modulus ($E_0$) and equilibrium

modulus ($E_3$) of shark hyaline cartilage were calculated to be about 5.6 MPa and 2 MPa, respectively.

Predication of relaxation data for tessellated cartilage under normal loading (TC NL) was first attempted using the present Maxwell/biphasic composite model based on the isostress condition using Eq. (17). Although high correlation coefficients ($R^2 > 0.99$; Table 2) were determined between the entire stress relaxation data sets and models, the calculated moduli of the tessellated layer exhibited high standard deviations, indicating that the Maxwell/biphasic composite model designed in the present work is not able to provide a consistent estimation of materials properties of the tessellated layer under normal loading. Rather, the biphasic model used to model non-tessellated cartilage seems to be applicable in this case, given the similarity in the shape of the relaxation curves for non-tessellated cartilage and tessellated cartilage under normal loading (Fig. 5). The accuracy of the biphasic model (dashed) for a representative relaxation response of tessellated cartilage under normal loading is demonstrated in Fig. 6b and associated regression results listed in Table 1.

Simulation of the time dependent response for tessellated cartilage under parallel loading (TC PL) was attempted using both the transversely isotropic biphasic model and the composite model derived in present work for isostrain conditions. Representative experimental data for the stress relaxation phase are plotted in Fig. 6(c) and Fig. 7(a)–(c), with corresponding regression results for composite models with one Maxwell element, two Maxwell elements and three Maxwell elements. We note that the plots in Fig. 7 focus on the first 500 s of stress relaxation where the most rapid transitions occur. The coefficients of determination listed in Tables 1 and 2 indicate that both the Maxwell/biphasic composite model and biphasic model exhibit good agreement with experimental data. However, the permeability predicted by the biphasic model ($9.93 \times 10^{-13}$ m$^4$/Ns) is approximately three orders of magnitude higher than that for typical mammalian hyaline cartilage and highly variable as indicated by the relatively large standard deviation ($10.7 \times 10^{-13}$ m$^4$/Ns). Thus, it appears that tessellated cartilage under parallel loading does not deform in a manner as mammalian hyaline cartilage that is described well by biphasic theory alone. Instead, moduli and permeabilities estimated from Maxwell/biphasic composite models are statistically more self-consistent as indicated by relatively small standard deviations compared to their corresponding mean values (Table 2). A comparison of the three iterations of composite models with the first 500 s of a
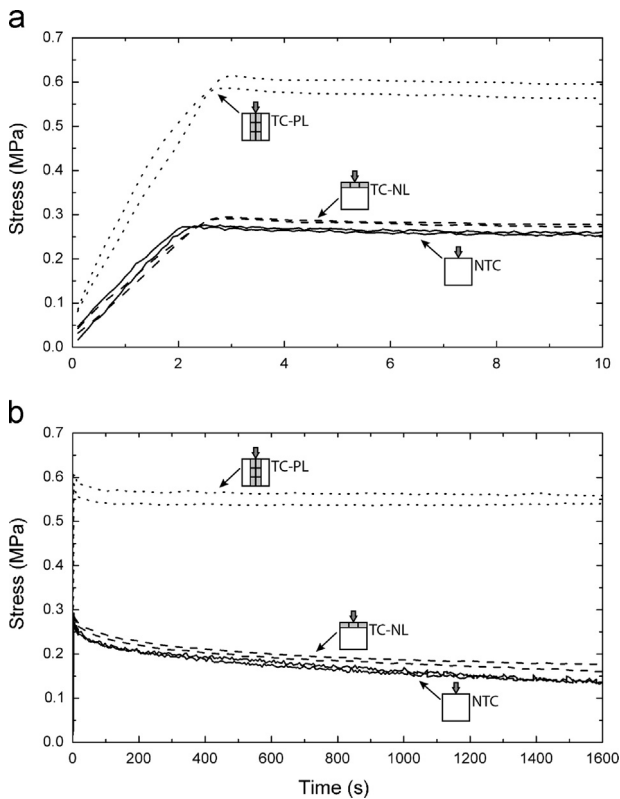


Fig. 5 – Ramp (a) and stress relaxation (b) curves for tessellated and uncalcified cartilage. NTC: non-tessellated cartilage, TC: tessellated cartilage, NL: loading normal to the tessellated layer, PL: loading parallel to the tessellated layer.

**Table 1 – Non-linear regression results for the transversely isotropic biphasic model for both shark non-tessellated cartilage and tessellated cartilage. NTC: non-tessellated cartilage, TC: tessellated cartilage, NL: loading normal to the tessellated layer, PL: loading parallel to the tessellated layer. The values and standard deviations listed correspond to the means of the best fit values for at least eight replicate experiments for each specimen type and loading direction.**

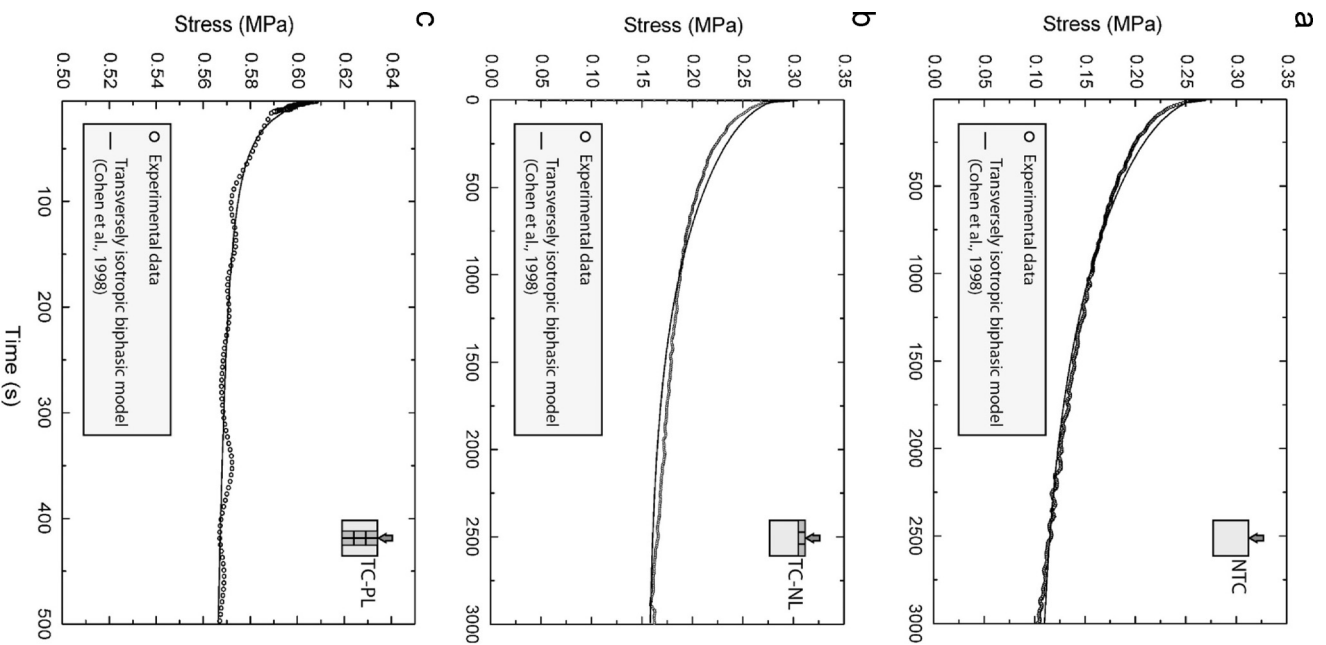| | NTC | TC-NL | TC-PL |
|---|---|---|---|
| $E_3$ (MPa) | $1.97 \pm 0.04$ | $2.75 \pm 0.25$ | $10.91 \pm 0.36$ |
| $E_1$ (MPa) | $0.15 \pm 0.05$ | $0.11 \pm 0.03$ | $2.01 \pm 0.87$ |
| $E_0$ (MPa) | $5.56 \pm 0.44$ | $6.13 \pm 0.73$ | $12.05 \pm 0.27$ |
| $\nu_{21}$ | $0.98 \pm 0.02$ | $1.01 \pm 0.01$ | $1.51 \pm 0.16$ |
| $\nu_{31}$ | $0.46 \pm 0.05$ | $0.34 \pm 0.05$ | $0.43 \pm 0.09$ |
| $k$ (m$^2$/Ns) | $8.79 \times 10^{-16} \pm 2.95 \times 10^{-16}$ | $1.28 \times 10^{-15} \pm 0.39 \times 10^{-15}$ | $9.93 \times 10^{-13} \pm 10.70 \times 10^{-13}$ |
| $R^2$ | 0.992 | 0.990 | 0.985 |

Fig. 6 – Representative relaxation response for shark (a) non-tessellated cartilage, (b) tessellated cartilage under parallel loading and (c) tessellated cartilage under parallel loading along with non-linear regression fits for the transversely isotropic biphasic model.

representative stress relaxation (Fig. 7), indicates that the three-element Maxwell/biphasic model is better at simulating the time-dependent behavior of tessellated cartilage under parallel loading over the most dynamic part of the loading history. By contrast, the one-element Maxwell/biphasic model gives predictions that have a relatively poor correlation with experimental data and the two-element Maxwell/biphasic model underestimates the initial response by 5%. The average instantaneous and equilibrium moduli of the tessellated

Table 2 – Non-linear regression results for composite models that combine a biphasic description of the hyaline component with a generalized Maxwell model of the tessellated layer. TC: tessellated cartilage, NL: loading normal to the tessellated layer, PL: loading parallel to the tessellated layer. The values and standard deviations listed correspond to the means of the best fit values for at least eight replicate experiments for each specimen type and loading direction.

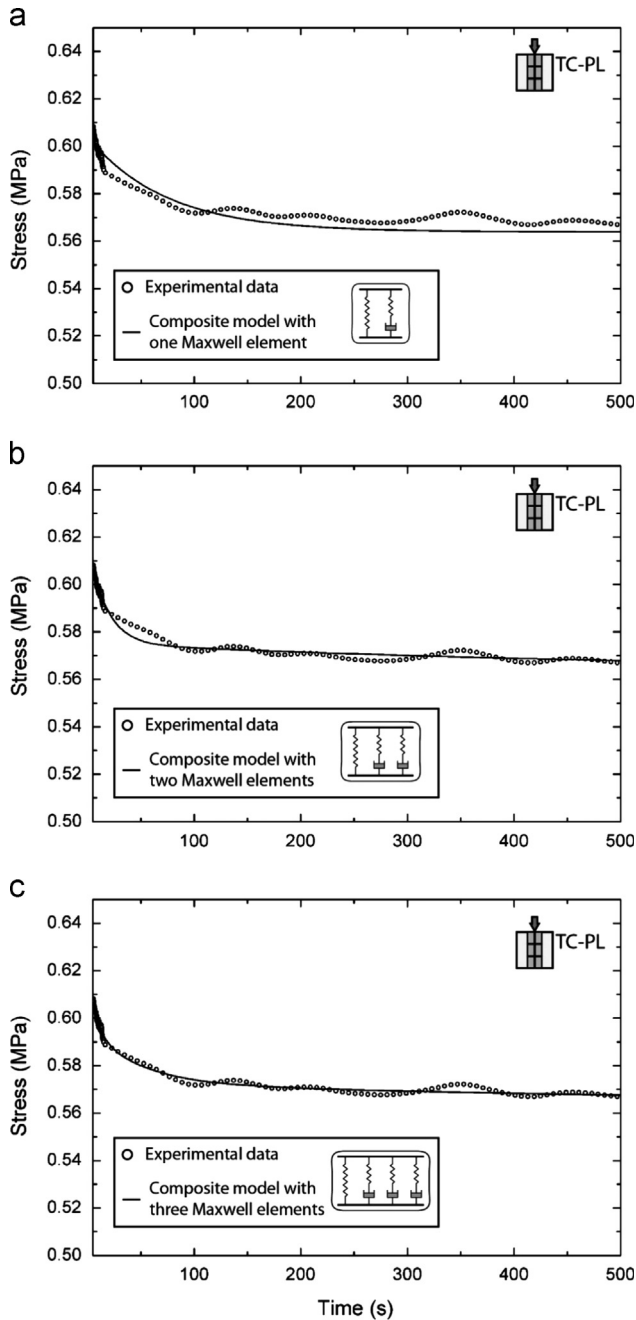| | TC NL | | | TC PL | | |
|---|---|---|---|---|---|---|
| | One Maxwell element | Two Maxwell elements | Three Maxwell elements | One Maxwell element | Two Maxwell elements | Three Maxwell elements |
| $E_0$ (MPa) | $3.85 \pm 2.28$ | $12.16 \pm 9.42$ | $12.36 \pm 9.95$ | $99.31 \pm 3.61$ | $101.1 \pm 3.34$ | $102.8 \pm 3.24$ |
| $E_\infty$ (MPa) | $1.93 \pm 1.20$ | $1.93 \pm 1.24$ | $1.88 \pm 1.28$ | $91.67 \pm 4.20$ | $91.43 \pm 4.03$ | $91.31 \pm 3.94$ |
| $P_1$ | $0.46 \pm 0.16$ | $0.62 \pm 0.21$ | $0.64 \pm 0.13$ | $0.08 \pm 0.01$ | $0.07 \pm 0.01$ | $0.05 \pm 0.01$ |
| $P_2$ | | $0.18 \pm 0.14$ | $0.14 \pm 0.07$ | | $0.02 \pm 0.02$ | $0.04 \pm 0.01$ |
| $P_3$ | | | $0.03 \pm 0.04$ | | | $0.02 \pm 0.01$ |
| $k$ (m$^2$/Ns) | $2.84 \times 10^{-16} \pm 1.02 \times 10^{-16}$ | $2.82 \times 10^{-16} \pm 1.03 \times 10^{-16}$ | $2.75 \times 10^{-16} \pm 1.03 \times 10^{-16}$ | $2.01 \times 10^{-11} \pm 0.81 \times 10^{-1}$ | $2.02 \times 10^{-11} \pm 0.81 \times 10^{-11}$ | $1.34 \times 10^{-11} \pm 0.27 \times 10^{-11}$ |
| $\tau_1$ | $132.7 \pm 56.6$ | $2.39 \pm 1.72$ | $1.73 \pm 0.36$ | $68.55 \pm 45.68$ | $17.66 \pm 6.24$ | $5.81 \pm 0.84$ |
| $\tau_2$ | | $148.5 \pm 59.4$ | $121.4 \pm 74.1$ | | $466.8 \pm 287.7$ | $51.49 \pm 19.96$ |
| $\tau_3$ | | | $683.7 \pm 369.1$ | | | $870.8 \pm 549.5$ |
| $R^2$ | 0.998 | 0.998 | 0.998 | 0.963 | 0.988 | 0.989 |

Fig. 7 – The first 500 s of a representative relaxation response for shark tessellated cartilage under parallel loading along with regression fits for the present composite model with (a) one Maxwell element, (b) two Maxwell elements and (c) three Maxwell elements.

layer predicted by the three-element composite models are greater than 101 MPa and 91 MPa, respectively, which are approximately 18 times and 45 times higher than those for non-tessellated cartilage. In addition, the average value for permeability of the tessellated cartilage predicted by the composite model was approximately by four orders of magnitude greater than that for typical hyaline cartilage ($10^{-15}$ to $10^{-16}$ m$^4$/Ns) (Mansour, 2003).

## 5.    Discussion

The present correlations between model predictions and experimental data demonstrated that the transversely isotropic biphasic model developed by Cohen et al. (1998) is adequate for an accurate representation of the viscoelastic behavior of uncalcified shark cartilage and tessellated cartilage under normal loading in stress relaxation tests. However, the biphasic model is not optimum for describing the behavior of tessellated cartilage when parallel loading is applied. Incorporation of the biphasic model into a generalized Maxwell model was found to be more effective for simulating the behavior of the tessellated cartilage for this loading direction. This finding can be understood by examining the differences in roles of the calcified and uncalcified cartilage under normal and parallel loading conditions. Since we would expect the tessellated layer and uncalcified cartilage to deform to different degrees in normal loading, and therefore to correspond to isostress conditions (Eq. (16)), and since the tessellated layer comprises a small portion of the overall tissue (volume fraction ~0.1), it follows that the effective elastic modulus of the tissue would be dominated by the less stiff hyaline cartilage. This explains the effective similarity in time-dependent properties for uncalcified cartilage and tessellated cartilage under normal loading (i.e. similarly accurate nonlinear regressions of experimental data by the biphasic model). The equilibrium and instantaneous modulus for tessellated cartilage under normal loading seem to be only slightly higher and the predicted Poisson's ratios and permeability are also similar. For this loading direction, the tessellated tissue essentially behaves as uncalcified cartilage in most aspects.

In contrast to normal loading, parallel loading gives rise to isostrain conditions governed by Eq. (17) which dictate that the substantially stiffer tessellated layer contributes more to the overall composite modulus. As a result, a composite model, combining the biphasic model with generalized Maxwell components (representing the hyaline cartilage and tessellated layer, respectively), more accurately described the relaxation behavior of the composite tissue. A composite model combining three-Maxwell elements with the biphasic model provided better agreement with experimental data than composite models with only one or two Maxwell elements describing the tessellated layer (Fig. 7(a)–(c)). The accuracy of the three-Maxwell element composite model could be a function of the three material types contributing to the viscoelastic relaxation behavior of the tessellated layer: the mineralized tissue in tesserae, the fiber joints between the tesserae, and the interstitial fluid distributed through both the mineralized and fibrous phases. It is also worth to notice that the stress relaxation curve for tessellated cartilage under parallel loading appears to oscillate somewhat irrationally, which is possibly a consequence of the settlement of joints in the tessellated layer. Liu et al. (2010) demonstrated that joints vary significantly in dynamic response within the tessellated layer and their influences on the overall relaxation behavior could be significant. So it is likely that that the relaxation response of joints may be responsible for the observed oscillations in the data. More work is needed to explore this possibility.

The present model also indicates that tessellated cartilage under parallel loading exhibits a much greater permeability and therefore reveals that the interstitial fluid is extruded more rapidly in the tessellated cartilage under parallel loading. In addition, although the average permeability value for uncalcified blue shark cartilage was determined to be $8.79 \times 10^{-16}$ m$^4$/Ns, within the range of typical values ($10^{-15}$ to $10^{-16}$ m$^4$/Ns) for mammalian cartilage, the average permeability of the tessellated cartilage predicted by the composite model was approximately by four orders of magnitude greater than that for typical hyaline cartilage (Mansour, 2003). These results indicate that the drag forces between the hyaline cartilage matrix and interstitial fluid are greatly diminished for deformation under parallel loading. This increase of permeability can be attributed to the fact that the tessellated layer supports most of the resulting stress under parallel loading, with the high permeability of tessellated cartilage in parallel loading likely a reflection of the high permeability of the tessellated layer itself: anisotropy in the freedom of fluid movement (in normal vs. parallel loading) is supported by a recent anatomical study revealing a network of passageways (canaliculi) extending through tesserae, connecting the cells entombed in the mineralized matrix (Dean et al., 2010). These intratesseral canaliculi radiate out from the center of each tessera, predominantly within the plane of the tesseral mat, not perpendicular to it (i.e. canals connect adjacent cells, not those above or below). As the canals perforate the mineralized tissue completely, opening into the joints connecting adjacent tesserae, interstitial fluid could conceivably flow easily within the plane of the tesseral mat, an arrangement that would increase the permeability of tessellated cartilage in parallel loading, and could also be vital for communication and the distribution of nutrients among cells.

There are currently no published data on elasmobranch unmineralized cartilage material properties, making it difficult to ground-truth our data with other studies. Our values for the elastic modulus of blue shark uncalcified cartilage (2 MPa), however, are similar to those reported for mammalian cartilages (0.45–19 MPa; Athanasiou et al., 1991; Mansour, 2003; Silver et al., 1992). Two as of yet unpublished datasets on elasmobranch cartilage report values, an order of magnitude higher than ours, from uncalcified jaw cartilage from two shark species tested in stress relaxation (*N. brevirostris, H. francisci*; 43–56 MPa; Huber, unpublished. data) and uncalcified jaw and chondrocranial cartilage plugs tested in unconfined compression (*Squalus acanthias*; 20–78 MPa for jaws, 116–775 MPa for chondrocranium; Porter et al., 2013). This suggests perhaps that the structure and modulus of uncalcified cartilage may vary to some degree across species and between different skeletal elements; investigations of species- and element-specific variation in tissue properties and relation to animal ecology (e.g. diet, swimming mode, habitat) will provide valuable insight into properties relevant to skeletal performance in this system.

The substantial difference between the modulus of the blue shark uncalcified cartilage and the tessellated layer indicated by the present models is reasonable considering the materials properties and volume fractions of tissues involved in the tessellated layer (Fung, 1993): the mineral component of the tesserae (carbonated apatite; Applegate, 1967) has a modulus that can exceed 100 GPa and the soft joint tissue between the tesserae only occupies only about 2% of tessellated layer (Dean et al., 2009; Liu et al., 2010). Tesserae exhibit a variety of geometric shapes, but are predominantly hexagonal (Dean et al., 2009); we note that only tesseral joints that are arranged in series with respect to the loading direction have a significant impact on the effective modulus of the tessellated layer (Liu et al., 2010). Accordingly, we substitute the effective equilibrium modulus of the tessellated layer ($E_{eff} \approx 91$ MPa) and the reference values of the elastic modulus of tesserae as well as the volume fraction of joints into Eq. (16). Rearranging terms, the resulting elastic modulus of the interstitial joints is calculated to be 1.8 MPa, in the lower end of the range of moduli for mammalian fibrous tissues (e.g. ligament; Donahue et al., 2003) and well beneath the threshold modulus predicted by Liu et al.'s (2010) analytical model for maintaining adequate flexibility in the tessellated layer to re-distribute damaging stresses away from tension-loaded areas of the skeleton.

Perhaps the most striking contribution the tessellated layer provides to the overall performance of the tissue is that it strongly increases both the instantaneous and equilibrium modulus of the composite structure, however only under parallel loading. This effect would result in much greater stiffness for loading in this direction; it is interesting to note in cross-sections of elasmobranch skeletons, particularly those with more limited loading directions (e.g. jaws, Fig. 8), material is typically arranged to maximize the portion of the tessellated layer under parallel loading orientation and minimize the portion arranged under normal loading. Such tissue arrangement would be particularly advantageous for portions of the skeleton experiencing relatively anisotropic and/or rapid loading: for example, the greater dynamic stiffness provided by the tessellated layer in parallel loading would be advantageous for mastication of prey, particularly those that are protected with a hard shell. By contrast, the dynamic stiffness normal to the tessellated layer is practically as low as that for hyaline cartilage so that a predatory or defensive strike in this direction would result in relatively modest stresses and therefore, have less potential for inducing damage to the tissue. The anisotropic stress relaxation response of tessellated shark cartilage therefore results in an inherent, "smart" management of loading stresses, likely extremely valuable to the fatigue resistance of this skeletal type.

Given the mechanical anisotropy we have shown for the tessellated cartilage system, the arrangement of tessellated tissue in a skeletal cross-section should provide clues to the loading regimes experienced by the animal in life. Given the lack of gravity experienced by cartilaginous fishes, we imagine their skeletons' primary loading mode to be bending. From an engineering standpoint, beams (or skeletal elements) with circular cross-sections provide the best resistance to multi-axial bending, whereas beams with elliptical cross-sections exhibit asymmetrical bending resistance and are stiffer when bending is in line with the cross-section's longest axis (as in the familiar example of an architectural I-beam) (Weaver and Ashby, 1997). Flexural stiffness of an element can also be increased through use of stiffer constituent materials (Weaver and Ashby, 1997); in the case
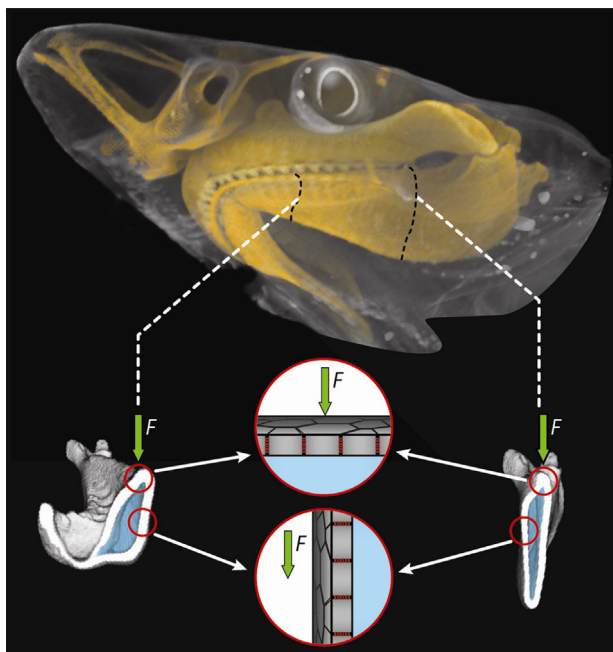
**Fig. 8 – Tesseral surface orientations in the jaws of the blue shark, *Prionace glauca*. In digital CT scan cross-sections from two locations in the lower jaw (left: from beneath the teeth; right: from area of muscle adductor attachment), mineralized material in the tessellated layer is white and the radiolucent uncalcified cartilage has been colored blue. Loading orientations applied in this study correspond to loading scenarios in vivo: in regions where the tessellated areas are oriented more horizontally, bite force would be applied in a direction "normal" to the tessellated layer (top schematic image), whereas regions with more vertical orientation would experience more in-plane "parallel" loading (bottom schematic image). (For interpretation of the references to color in this figure legend, the reader is referred to the web version of this article.)**

locomotory mode. Observed differences in skeletal flexural stiffness across the five species examined were dictated by the geometric arrangement (and to some degree, the level of mineralization) of the tessellated layer, rather than by changes in thickness of tesserae (Macesic and Summers, 2012). This demonstration of the link between morphology and skeletal performance underlines the importance of the basic tissue anisotropy, shown by our data, in determination of whole element biomechanics in the tessellated skeletal system.

Such a fundamental structure–function relationship – wherein gross skeletal geometry reflects loading direction – is well-known for bone, where skeletal architecture, geometry and composition can adapt in response to both the magnitude and orientation of mechanical loads (Burr et al., 2002; Ruff et al., 2006; Seeman, 2009). Tessellated cartilage, however, apparently cannot perform the fundamental remodeling and modeling processes that allow bones to adapt to loading conditions; therefore (non-pathologic) skeletal geometries are genetically predetermined, not environmentally shaped (Summers, 2000; Ashhurst, 2004). Given this ontogenetic constraint on skeletal shape, in the case of elliptical skeletal cross-sections (e.g. the extremely compressiform jaw section to the right in Fig. 8), potentially dangerous off-axis loads must be kept to a minimum, either by stereotyped muscle contraction patterns and/or inherent aspects of skeletal architecture (e.g. specific tesseral tiling patterns allowing some skeletal deformations but not others). Further analyses of tessellated cartilage morphology and mechanics in the contexts of organismal performance and behavior will provide vital insight into the roles of the tissue phases in this tiled composite material.

## 6.    Conclusion

Stress relaxation data were generated for tessellated and uncalcified cartilage tissue from the jaws of blue sharks. The experimental results for the uncalcified cartilage sample were found to agree reasonably well with behavior predicted by a transversely isotropic biphasic model. Incorporation of this biphasic approach into a generalized Maxwell model provides more accurate simulations of the behavior of tessellated tissue when loaded parallel to the plane of the tesserae. This is a reasonable finding considering the tessellated layer's contribution to stiffness and constraint of the soft tissue under parallel loading. However, the generalized Maxwell model does not provide a better description of the behavior of calcified cartilage under loading normal to the plane of the tessellated layer. This result is consistent with the fact that the role of the tessellated layer is much less significant under loading in this direction. As a result, there was a relatively small difference between the viscoelastic behaviors of tessellated cartilage under loading normal to the plane of the tissue compared to uncalcified cartilage. In sum, the present results indicate that the tessellated layer provides anisotropic compressive stiffness and that the tissue may be arranged in ways to take the most advantage of this effect, with parallel-loaded tesserae positioned in areas requiring relatively high forces (e.g. beneath the teeth of the jaw) and normal-loaded

of composite tissues with anisotropic bending resistance, however, a given tissue morphology can provide a range of flexural stiffnesses dependent on the tissue arrangement relative to the primary direction of loading.

If the inherent anisotropy of the tesserae-cartilage composite plays an in vivo role in skeletal stiffening, we would expect regions with anisotropic loading direction to exhibit elliptical skeletal cross-sections, with the predominant loading direction being the one where the most tesserae are loaded in the plane of the tesseral mat ("parallel loading" orientation). Such an arrangement would exploit the anisotropy of tessellated cartilage at the tissue level, while also increasing the second moment of area and bending resistance of the whole cross-section by arranging the majority of material in line with skeletal bending. This hypothesis is supported by Macesic and Summers' study, showing that the cross-sectional shape of tessellated pelvic skeletal elements in ray species varied predictably according to the degree to which they use the elements to push along the seafloor, with more elliptical cross-sections reflecting a predominant pushing direction for species that rely more on this particular

tesserae, which have little effect in increasing stiffness, in areas where load-damping may be more important.

## Acknowledgment

REFERENCES

Applegate, S.P., 1967. A survey of shark hard parts. In: Gilbert, P.W., Mathewson, R.F., Rall, D.P. (Eds.), Sharks, Skates and Rays. Johns Hopkins Press, Maryland, pp. 37–66.

Armstrong, C.G., Lai, W.M., Mow, V.C., 1984. An analysis of the unconfined compression of articular cartilage. Journal of Biomechanical Engineering 106, 165–173.

Ashhurst, D.E., 2004. The cartilaginous skeleton of an elasmobranch fish does not heal. Matrix Biology 23, 15–22.

Athanasiou, K.A., Rosenwasser, M.P., Buckwalter, J.A., Malinin, T.I., Mow, V.C., 1991. Interspecies comparisons of in situ intrinsic mechanical properties of distal femoral cartilage. Journal of Orthopaedic Research 9, 330–340.

Brinson, H.F., Brinson, L.C., 2007. Engineering Science and Viscoelasticity. Springer, New York171–172.

Burr, D.B., Robling, A.G., Turner, C.H., 2002. Effects of biomechanical stress on bones in animals. Bone 30, 781–786.

Chen, T., 2000. Determining a Prony Series for a Viscoelastic Material from Time Strain Data. NASA/TM-2000-210123.

Clement, J.G., 1992. Re-examination of fine structure of nendoskeletal mineralization in chondricthyes: implications for growth, aging, and calcium Homeostasis. Australian Journal of Marine & Freshwater Research 43, 157–181.

Cohen, B., Lai, W.M., Mow, V.C., 1998. A transversely isotropic biphasic model for unconfined compression of growth plate and chondroepiphysis. Journal of Biomechanical Engineering 120, 491–496.

Cohen, B., Gardner, T.R., Ateshian, G.A., 1993. The influence of transverse isotropy on cartilage indentation behavior. A study on the human humeral head. Transactions of Orthopaedic Research Society 18, 185.

Dean, M.N., Summers, A.P., 2006. Mineralized cartilage in condrichthyan fishes. Zoology 109, 164–168.

Dean, M.N., Mull, C.G., Gorb, S.N., Summers, A.P., 2009. Ontogeny of the tessellated skeleton: insight from the skeletal growth of the round stingray *Urobatis halleri*. Journal of Anatomy 215, 227–239.

Dean, M.N., Socha, J.J., Hall, B.K., Summers, A.P., 2010. Canaliculi in the tessellated skeleton of cartilaginous fishes. Journal of Applied Ichthyology 26, 263–267.

Dingerkus, G., Seret, B., Guilbert, E., 1991. Multiple prismatic calcium phosphate layers in the jaws present-day sharks. Experientia 47, 38–40.

Donahue, T.L.H., Hulla, M.L., Rashid, M.M., Jacobs, C.R., 2003. How the stiffness of meniscal attachments and meniscal material properties affect tibio-femoral contact pressure computed using a validated finite element model of the human knee joint. Journal of Biomechanics 36, 19–34.

Fix, D., Weinkamer, R., Fratzl, P., Dean, M.N., 2013. Micrometer-scale material characterization of mineralized elasmobranch cartilage: a novel combination of nanoindentation and scanning acoustic microscopy, in preparation.

Fung, Y.C., 1993. Biomechanics: Mechanical Properties of Living Tissues. Springer, New York503.

Hacker, C.L., Ansell, M.P., 2001. Fatigue damage and hysteresis in wood-epoxy laminates. Journal of Materials Science 36, 609–621.

Hall, B.K., 2005. Bones and Cartilage: Developmental Skeletal Biology. Elsevier/Academic Press, London.

Huber, D.R., 2006. Cranial biomechanics and feeding performance of sharksDepartment of Biology, University of South Florida, Tampa, FL250.

Huber, D.R., Eason, T.G., Hueter, R.E., Motta, P.J., 2005. Analysis of the bite force and mechanical design of the feeding mechanism of the durophagous horn shark *Heterodontus francisci*. Journal of Experimental Biology 208, 3553–3571.

Hunziker, E.B., 1999. Articular cartilage repair: are the intrinsic biological constraints undermining this process insuperable? Osteoarthritis Cartilage 7, 15–28.

Kemp, N.E., Westrin, S.K., 1979. Ultrastructure of calcified cartilage in the endoskeletal tesserae of sharks. Journal of Morphology 160, 75–102.

Kinney, J.H., Marshall, S.J., Marshall, G.W., 2003. The mechanical properties of human dentin: a critical review and re-evaluation of the dental literature. Critical Reviews in Oral Biology & Medicine 14 (1), 13–29.

Lakers, R.S., Vanderby, R., 1999. Interrelation of creep and relaxation: a modeling approach for ligaments. Journal of Biomechanics 121 (6), 612–615.

LeRoux, M.A., Setton, L.A., 2002. Experimental and biphasic FEM determinations of the material properties and hydraulic permeability of the meniscus in tension. Journal of Biomechanics 124, 315–321.

Liu, X., Dean, M.N., Summer, A.P., Earthman, J.C., 2010. Composite model of the shark's skeleton in bending: a novel architecture for biomimetic design of functional compression bias. Materials Science and Engineering C 30, 1077–1084.

Lu, X.L., Miller, C., Chen, F.H., Guo, X.E., Mow, V.C., 2007. The generalized triphasic correspondence principle for simultaneous determination of the mechanical properties and proteoglycan content of articular cartilage by indentation. Journal of Biomechanics 40, 2434–2441.

Macesic, L.J., Summers, A.P., 2012. Flexural stiffness and composition of the batoid propterygium as predictors of punting ability. The Journal of Experimental Biology 215, 2003–2012.

Mak, A.F., 1986. The apparent viscoelastic behavior of articular cartilage—the contributions from the intrinsic matrix viscoelasticity and interstitial fluid flows. Journal of Biomechanical Engineering 108, 123–130.

Mak, A.F., Mow, V.C., 1987. Biphasic indentation of articular cartilage-1. Theoretical analysis. Journal of Biomechanics 20, 703–714.

Malzahn, J.C., Schultz, J.M., 1986. Tension–tension and compression–compression fatigue behavior of an injection-molded short-glass-fiber/poly(ethylene terephthalate) composite. Composites Science and Technology 27, 253–289.

Mansour, J.M., 2003. Biomechanics of cartilage. In: Oatis, C.A. (Ed.), Kinesiology: the Mechanics and Pathomechanics of Human Movement. Lippincott Williams and Wilkins, Philadelphia (Chapter 5), pp. 66–79.

Mow, V.C., Gibbs, M.C., Lai, W.M., Zhu, W.B., Athanasiou, K.A., 1989. Biphasic indentation of articular Cartilage-2. A numerical algorithm and an experimental study. Journal of Biomechanics 22, 853–861.

Mow, V.C., Kuei, S.C., Lai, W.M., Armstrong, C.G., 1980. Biphasic creep and stress relaxation of articular cartilage in

compression: theory and experiments. Journal of Biomechanical Engineering 102, 73–84.

Moss, S.A., 1977. Skeletal tissues in sharks. American Zoologist 17, 335–342.

Porter, M.E., Beltrán, J.L., Kajiura, S.M., Koob, T.J., Summers, A.P., 2013. Stiffness without mineral: material properties and biochemical components of jaws and chondrocrania in the Elasmobranchii (sharks, skates, and rays). PeerJ., Submitted.

Roylance, D., 2001. Engineering Viscoelasticity, p. 14–15.

Ruff, C., Holt, B., Trinkaus, E., 2006. Who's afraid of the big bad Wolff?: 'Wolff's law' and bone functional adaptation. American Journal of Physical Anthropology 129, 484–498.

Seeman, E., 2009. Bone modeling and remodeling. Critical Reviews in Eukaryotic Gene Expression 19, 219–230.

Shepherd, T.N., Zhang, J., Ovaert, T.C., Roeder, R.K., Niebur, G.L., 2011. Direct comparison of nanoindentation and macroscopic measurements of bone viscoelasticity. Journal of the Mechanical Behavior of Biomedical Materials 4, 2055–2062.

Silver, F.H., Kato, Y.P., Ohno, M., Wasserman, A.J., 1992. Analysis of mammalian connective tissue: relationship between hierarchical structures and mechanical properties. Journal of Long-Term Effects of Medical Implants 2, 165–198.

Suh, J.K., Bai, S., 1998. Finite element formulation of biphasic poroviscoelastic model for articular cartilage. Journal of Biomechanical Engineering 120, 195–201.

Summers, A.P., 2000. Stiffening the stingray skeleton - An investigation of durophagy in myliobatid stingrays (Chondrichthyes, Batoidea, Myliobatidae). Journal of Morphology 243, 113–126.

Weaver, P.M., Ashby, M.F., 1997. Material limits for shape efficiency. Progress in Materials Science 41, 61–128.

Wroe, S., Huber, D.R., Lowry, M.B., McHenry, C.R., Moreno, K., Clausen, P.D., Ferrara, T.L., 2008. Three-dimensional computer analysis of white shark jaw mechanics: how hard can a great white bite? Zoology 276, 336–342.

Yin, L., Elliott, D.M., 2004. A biphasic and transversely isotropic mechanical model for tendon: application to mouse tail fascicles in uniaxial tension. Journal of Biomechanics 22 (927-916).

Zhang, M., Guo, X., Kassab, G.S., 2008. A generalized Maxwell model for creep behavior of artery opening angle. Journal of Biomechanical Engineering 130, 054502.